Taylor & Francis
Taylor & Francis Group

ORIGINAL ARTICLE

Axial-shear interaction effects on microdamage in bovine tibial trabecular bone

XIANG WANG, JACQUES GUYETTE, XIANGYI LIU, RYAN K. ROEDER, & GLEN L. NIEBUR

Tissue Mechanics Laboratory, Department of Aerospace and Mechanical Engineering, University of Notre Dame, Notre Dame, IN 46556, USA

Abstract

Because many osteoporotic fractures occur during a fall, understanding the effect of off-axis loads on initiation and propagation of microdamage in trabecular bone should provide further insight into the biomechanics of age-related fractures. Fourteen on-axis cylindrical specimens were prepared from 12 bovine tibiae. Fluorescent stains were used to label the microdamage due to a sequence of compressive and torsional damaging loads. The mean decrease in Young's modulus was over four times greater than that in the shear modulus after the compressive overload, while there was no difference between the decrease in the axial and torsional stiffnesses after the torsional overload. The total microcrack density due to compression was uniform across the radius of the cylindrical specimens, while the mean density of microcracks due to torsional overloading increased from the axis of the cylindrical specimen to the circumference. The high density of microcracks near the axis of the specimen following torsional overloading was unexpected because of the low strains. Nearly 40% of the microcracks due to torsion propagated from pre-existing microcracks caused by axial compression, indicating that existing microcracks may extend at relatively low strain if the loading mode changes. The propagating microcracks were, on average, longer than the initiating microcracks due to either compressive or torsional loading. Damage due to axial compression appears to increase the susceptibility of trabecular bone to damage propagation during subsequent torsional loads, but it has little effect on the elastic properties in shear.

Keywords: *Microcracks, cancellous bone, propagation, compression, torsion*

Introduction

Microdamage, in the form of diffuse damage and microcracks, occurs in trabecular bone in vivo (Wenzel et al. 1996; Mori et al. 1997; Fazzalari et al. 1998a) and can be induced in vitro by fatigue or monotonic overloading (Fyhrie & Schaffler 1994; Wachtel & Keaveny 1997; Yeni et al. 2003). The use of bisphosphonates to treat osteoporosis can cause a further increase in microdamage accumulation in vivo, as they suppress the normal repair mechanism of remodeling (Mashiba et al. 2000, 2001). The presence of microdamage decreases the elastic modulus and energy to failure in trabecular bone (Keaveny et al. 1994b; Arthur Moore & Gibson 2002), and the maximum load and energy to failure in whole bones (Hoshaw et al. 1997). Because fractures of the proximal femur are most often due to a fall (Gregg et al. 1997; Fuller 2000; Gregg et al.

2000), understanding the accumulation of microdamage during off-axis loading should provide further insight into the biomechanics of age-related fractures and their relationship to damage accumulation.

Microdamage accumulation in trabecular bone during uniaxial compression and fatigue has been studied both in vitro and in vivo. During monotonic compression, the microcrack density, the total crack length, the number of damaged trabeculae and the total damaged area increase with increasing maximum strain (Wachtel & Keaveny 1997; Fazzalari et al. 1998a; Arthur Moore & Gibson 2002). The ultimate strain is higher in specimens that accumulate higher densities of microdamage (Fazzalari et al. 1998a), suggesting that the initiation of microcracks dissipates energy and increases energy to failure. Microcrack density increased with donor age and with decreasing volume fraction following compres-

sive testing of trabecular bone from the human femoral neck (Fazzalari et al. 1998b). The in vivo microcrack density is also inversely correlated with volume fraction (Yeni et al. 2003), and increases with increasing variability in trabecular tissue shear stress (Yeni et al. 2003). By contrast, diffuse damage does not depend on volume fraction or age *in vivo* (Vashishth et al. 2000). These studies suggest that changes in trabecular architecture related to aging increase susceptibility to microcrack accumulation, but do not affect diffuse damage accumulation. Microdamage has a detrimental effect on the mechanical properties of trabecular bone, with both the elastic modulus and the energy to failure decreasing following a damaging load (Keaveny et al. 1994b; Arthur Moore & Gibson 2002). The changes in the mechanical properties depend on the orientation of the damaging load and subsequent loads with respect to the trabecular architecture (Fazzalari et al. 1998a; Liu et al. 2003). As such, the interaction of sequential loads of differing modes or orientations may affect microdamage formation and the associated changes in mechanical properties in trabecular bone.

By employing differential staining techniques, it is possible to label microdamage due to each of a sequence of loads and study the initiation and propagation. The goal of this study was to investigate the interactions between damage induced by axial compression followed by shear overloading including microdamage accumulation and mechanical property changes. Specifically the objectives were to: (1) determine the relative reduction in the Young's and shear moduli of trabecular bone due to on-axis compressive overloading followed by torsional overloading; (2) quantify the microdamage associated with each loading mode; and (3) quantify the density and lengths of initiating and propagating microcracks that occur during an off-axis damaging load following a previous on-axis damaging load.

Methods

Specimen preparation

Fourteen on-axis cylindrical specimens were prepared from 12 bovine tibiae. The orientation of the specimens was controlled using micro-CT imaging. Briefly, the proximal tibia was sectioned into parallelepipeds that were later scanned at 60 μm resolution in a micro-CT scanner (μCT 80MG, Scanco Medical AG, Bassersdorf, Switzerland). They were saturated in a solution of 40% ethanol and 60% buffered saline during scanning in order to minimize changes in mechanical properties (Linde & Sorensen 1993). High-resolution finite element models were generated from the CT images and used to calculate the principal mechanical axes of the specimen (Van Rietbergen et al. 1996). Cylindrical specimens were cored along the principal orientation with a diamond coring drill (Starlite Industries, Bryn Mawr, PA). This procedure produces specimens with an average misalignment between the specimen and principal material axes of less than 5° (Wang et al. 2004). The specimens were approximately 8.2 mm in diameter and between 18 and 22 mm long.

The marrow was removed from the specimens in order to facilitate staining of microdamage with fluorescent dyes. A water jet was used to remove the marrow while the specimen was submerged in water to avoid damage to the trabeculae. Removing the marrow should not affect the mechanical properties at the strain rate used here (Carter & Hayes 1977). The prepared specimens were wrapped in gauze, hydrated with buffered saline solution, and stored at $-20°$C in airtight bags or containers except during staining and mechanical testing.

Damage staining

Prior to compressive mechanical testing, each specimen was stained in a solution of 0.5 mM alizarin complexone (ICN Biomedicals Inc., Aurora, OH) (O'Brien et al. 2002, 2003) to label microdamage incurred *in vivo* or during specimen preparation. Damage due to compressive overloading was labeled by soaking in a solution of 0.5 mM xylenol orange (Acros Organics, NJ) (O'Brien et al. 2002, 2003). After torsional testing, microdamage was labeled by soaking in a solution of 0.5 mM calcein (ICN Biomedicals) (O'Brien et al. 2002, 2003). Specimens were stained for 2 h in each step, and afterward the excess staining solution was removed by rinsing in deionized water.

Mechanical testing

Mechanical testing was performed under strain control on an Instron model 8821s bi-axial servo-hydraulic load frame (Instron Corp., Canton, MA, Figure 1). Specimens were embedded in brass endcaps, which were subsequently clamped into the load frame (Keaveny et al. 1997). The exposed length of the specimen was about half of its total length. The strain was measured with an axial/torsional extensometer (model 3550, Epsilon Technology Corp., Jackson, WY) attached to the endcaps. The effective gage length was taken as the exposed plus half the embedded length of the specimen for axial loading (Keaveny et al. 1997) and the exposed length for torsional loading (Fenech & Keaveny 1999). All tests were performed at room temperature, and the exposed portion of the specimen was
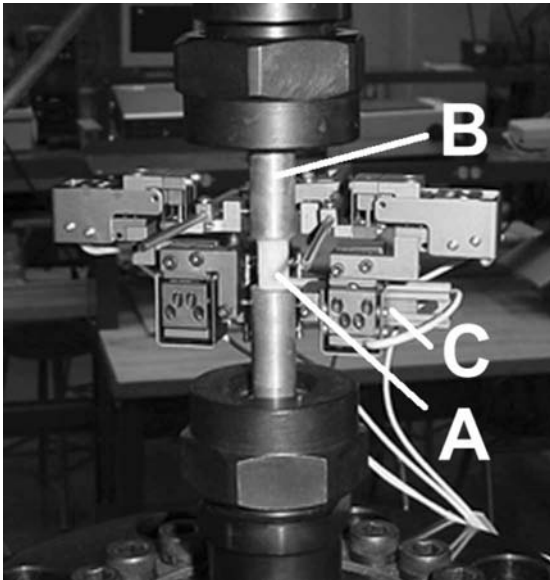
Figure 1. The trabecular bone specimen (A) was embedded in endcaps (B), which were fixed in grips. A bi-axial extensometer (C) was attached to the endcaps. The upper grip was fixed during testing. The lower grip can move vertically or rotationally to apply compressive or torsional loading to the specimen, respectively. Gauze saturated in saline was wrapped around the exposed portion of the specimen to keep it hydrated (removed for illustration purposes).

Figure 2. Typical stress–strain curves from compressive overloading and unloading (a) and shear overloading (b). The dashed line is used to determine the 0.2% offset yield point.

wrapped with gauze saturated in buffered saline solution to keep the bone hydrated during testing.

The undamaged Young's and shear moduli of each specimen were measured non-destructively. The specimens were loaded in on-axis compression from 0 to 0.4% strain three times at a strain rate of 0.2% per second. This is below the elastic limit strain of bovine tibial trabecular bone. As such, no damage was expected to occur (Arthur Moore & Gibson 2002). Next, the specimens were loaded three times from 0 to 0.7% shear strain at the surface at a strain rate of 0.2% per second. Again, this is less than the shear elastic limit strain (0.97 ± 0.23%) for this type of bone in torsion (Ford & Keaveny 1996) such that no damage will develop. The undamaged Young's modulus, E_o, and shear modulus, G_o, were calculated from a second order polynomial fit to the data over a strain range from 0 to 0.2% or 0.4%, respectively (Morgan & Keaveny 2001).

The specimens were first damaged by monotonic overloading in compression. The specimens were compressed to 2% strain and immediately unloaded to zero load at a rate of 0.2% per second (Figure 2a). They were then removed from the load frame and stained in xylenol orange to label the microdamage that occurred during compression. After staining, the specimens were again mounted in the load frame, and the damaged axial and shear moduli were measured from three non-destructive loading cycles.
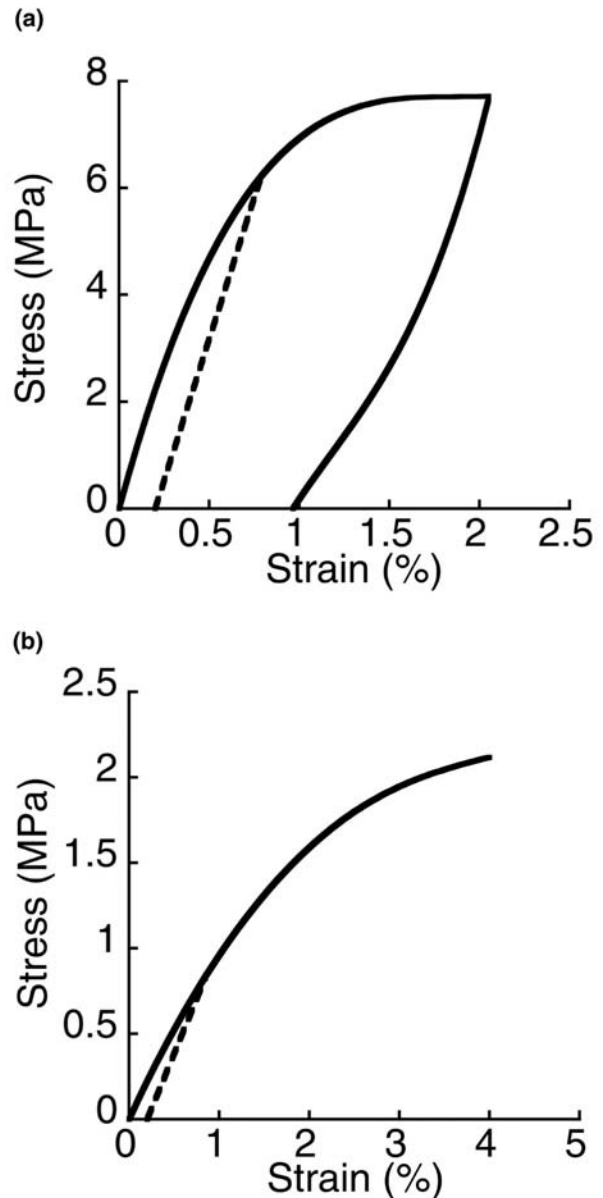
A pilot study showed that there was no change in the elastic modulus during the treatment with xylenol orange.

The specimens were further damaged in shear by a torsional load. They were overloaded in torsion to 4% shear strain at the surface and unloaded to zero torque at a strain rate of 0.2% per second (Figure 2b). The axial and torsional stiffness following shear damage were measured from the load–displacement curve and torque–twist curve, respectively. After torsional overloading, the specimens were stained in calcein to label the microdamage that occurred during torsion. The 0.2% offset yield points were calculated from the axial and shear stress–strain

curves during overloading. In torsion, a non-linear, time-independent model was used to convert the monotonic torque – twist curve to a shear stress – strain curve (Nadai 1950), as has been described by previous authors (Ford & Keaveny 1996). Because the damage accumulation was inhomogeneous following torsional loading due to increasing damage from the axis to the circumference, the damaged Young's and shear moduli were not calculated.

The trabecular architecture of the specimens was quantified using micro-CT. After mechanical testing, the specimens were scanned at 20 μm resolution while saturated in a solution of buffered saline and ethanol. The standard architectural parameters were quantified using the analysis application from the micro-CT scanner (μCT Evaluation program V4.3, Scanco Medical AG, Bassersdorf, Switzerland, Table I). The apparent density of the specimens was also calculated as the wet mass divided by bulk volume, and the volume fraction and tissue density were calculated using Archimedes' principle (Galante et al. 1970).

Damage quantification

Thin sections of the specimens were created for microscopic observation of microdamage. First, the specimens were gradually dehydrated in 70, 80 and 90% ethanol solutions (Lee et al. 1998) for 2 h per step and then soaked in 100% ethanol overnight. The dehydrated specimens were embedded in transparent methyl methacrylate (MMA, Aldrich Chemical Company, Inc., Milwaukee, WI) in a vacuum chamber. The embedded cylindrical cores were cut into 200-μm thick sections along their axes using a diamond saw (Arthur Moore & Gibson 2002). The surfaces of the sections were polished with a series of abrasives beginning with 600 grit paper and ending with $\frac{1}{4}$ μm diamond paste (Phoenix Beta, Buehler, Lake Bluff, IL). The final thickness of

Table I. The trabecular architecture of the specimens quantified using micro-CT ($n = 14$)

Parameters[a]	Mean	S.D.	Range
VF[b]	0.236	0.041	0.190 – 0.320
Tb.N (1/mm)	1.557	0.192	1.329 – 0.320
Tb.Th. (mm)	0.187	0.030	0.133 – 0.235
Tb.Sp. (mm)	0.608	0.068	0.467 – 0.700
SMI	0.861	0.610	– 0.131 – 2.169
Conn.D. (1/mm³)	5.180	2.276	2.610 – 11.45
DA	2.159	0.448	1.557 – 3.258

[a]VF = volume fraction; Tb.N. = trabecular number; Tb.Th. = trabecular thickness; Tb.Sp. = trabecular spacing; SMI = structural model index; Conn.D. = connectivity density; and DA = degree of anisotropy.
[b]Measured by Archimedes' Principle.

the polished sections was approximately 150 μm. The polished sections were mounted on glass slides using Eukitt's mounting medium (Calibrated Instruments, Inc., Hawthorne, NY) and glass cover slips. Three sections were obtained from each of eight specimens, two sections from five specimens, and four from another (34 total sections). Results from all sections from a single specimen were aggregated.

Microdamage was observed under ultraviolet epifluorescence microscopy with an excitation wavelength of 365 nm (UV-1A filter, Eclipse ME 600, Nikon Inc., Melville, NY). Diffuse damage appeared as regions of stained bone with irregular edges, while microcracks exhibited distinct edges and showed permeation of stain into the bone (Fazzalari et al. 1998b; Fyhrie & Schaffler 1994; Wachtel and Keaveny 1997). A 0.4-mm wide region at each end of the specimen was not analyzed to avoid measuring damage introduced during the sectioning procedure (Vashishth et al. 2000). Approximately 72, 1×1 mm square images from each thin section were captured at $\times 100$ magnification using a CCD camera attached to a personal computer (Magnafire Model S99806, Olympus America, Melville, NY). The images of the complete section were composited using image processing software (Adobe Photoshop 7.0, Adobe Systems Inc., San Jose, CA).

Each composite image was divided into three longitudinal regions according to the distance from cylindrical axis of the specimen (Figure 3). The inner region was within one-third of the radius from the specimen axis, the intermediate region between one-third and two-thirds of the radius, and the outer region was beyond two-thirds of the radius from the axis. Five sections were cut far enough from the axes of the specimens that they did not pass through the inner third of the radius. These were divided into only intermediate and outer regions. At least one inner, intermediate, and outer region was analyzed for each specimen.

Specialized image processing software (ImageTool Ver. 3.0, UTHSCSA, San Antonio, TX) was used to measure the bone area (B.Ar.), the number of microcracks (Cr.N.), the density of microcracks (Cr.Dn., mm^{-2}), the microcrack length (Cr.Ln., μm), and the diffuse damage area (Dx.Ar., mm^2/mm^2). The image of the section was displayed on the computer screen, and the bone area and the diffuse damage area were obtained by calculating the area of a surrounding polygon, whose edges were traced with the computer mouse. Similarly, the visible microcracks were traced using the mouse. The program assigned a number to each traced microcrack or diffuse damage area and recorded its length or area and staining color. Microcracks stained with a single fluorochrome initiated and formed during a
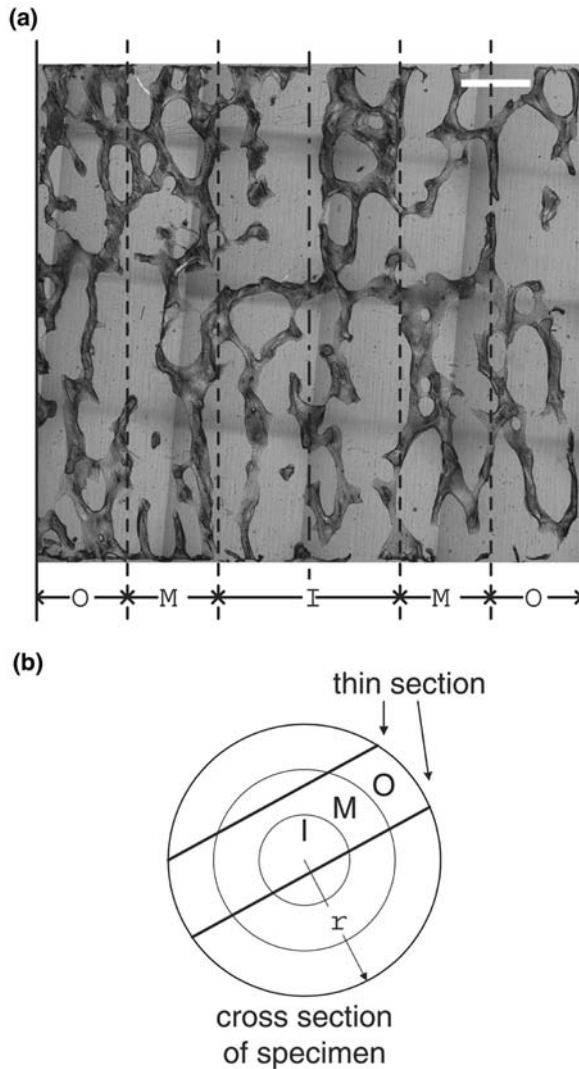
(a)

(b)

Figure 3. Thin sections were cut from the specimen near the cylindrical axis (a). Scale bar = 1 mm. Each section was divided into inner (I), intermediate (M), and outer (O) regions based on the distance from the cylindrical axis (b). If the section did not pass through the axis, the areas of regions were adjusted accordingly.

single loading model, while microcracks stained by both xylenol orange and calcein initiated during compression and propagated during torsional overloading (Figure 4). The propagating microcracks were counted and measured separately from singly stained cracks. The microcrack density (Cr.Dn.) was calculated by dividing the number of microcracks (Cr.N.) by the area of bone within the region (B.Ar.).

Statistical analysis was performed with JMP (JMP IN 5.1, SAS Institute Inc., Cary, NC) with a significance level of $p = 0.05$.

Results

To verify that no damage occurred during the initial modulus measurements, the Young's moduli calculated from the three nondestructive cycles and that calculated from the initial portion of the overloading stress–strain curve were compared by ANOVA. No difference was found ($p = 0.99$). Similarly, the shear modulus measured from the initial portion of torsional overloading was compared with the shear moduli measured from the three nondestructive cycles following compressive overloading but prior to shear overloading. Again, there was no difference ($p = 0.99$). As such, we assumed that no damage occurred during the modulus measurement. During the two compressive and torsional overloads, the maximum applied strains of 2.0 and 4.0% were higher than the measured 0.2% offset yield strains of $0.63 \pm 0.11\%$ and $1.23 \pm 0.34\%$, respectively.

Both the Young's and shear moduli decreased for 13 of 14 specimens following compressive overloading. The moduli of one specimen increased following testing. We chose not to discard the specimen, as we could not identify any error in the experiment or preparation. The mean undamaged and damaged Young's moduli were 1149 ± 400 and 1009 ± 394 MPa (mean $\pm$ standard deviation), respectively ($p = 0.009$, paired t-test). On average, Young's modulus decreased by $12.1 \pm 11.0\%$ following the compressive overload ($p = 0.003$, Wilcoxon signed rank test, Figure 5). The relative decrease did not depend on the volume fraction, or any architectural parameters ($p > 0.3$). The mean shear moduli before and after compressive overloading were 183 ± 75 and 179 ± 80 MPa ($p = 0.29$). On average, the relative change in the shear modulus was $2.47 \pm 4.68\%$ ($p = 0.011$). The dependence of the Young's and shear moduli on volume fraction did not change following compressive overloading ($p > 0.7$, ANCOVA, Figure 6). Following torsional overloading, the axial and torsional stiffnesses decreased $5.34 \pm 5.55\%$ ($p = 0.002$) and $6.35 \pm 5.07\%$ ($p = 0.001$), respectively. There was no difference between the decrease in the axial and torsional stiffnesses ($p = 0.42$, Wilcoxon test).

There was almost no measurable microdamage stained with alizarin. The mean density of microcracks stained was 0 in 13 of 14 specimens, and less than $0.05 \ \mathrm{mm}^{-2}$ in the other. As such, the specimen preparation and scanning did not induce significant damage in the specimens.

The microdamage due to compressive overloading was uniform across the specimen, while that due to torsional overloading increased from the axis to the circumference. The mean density of microcracks formed during compressive loading, including those that subsequently propagated during torsion, was $4.34 \pm 1.97 \ \mathrm{mm}^{-2}$ independent of region ($p = 0.25$, two-factor ANOVA, Figure 7a). The density of microcracks due to torsional overloading increased
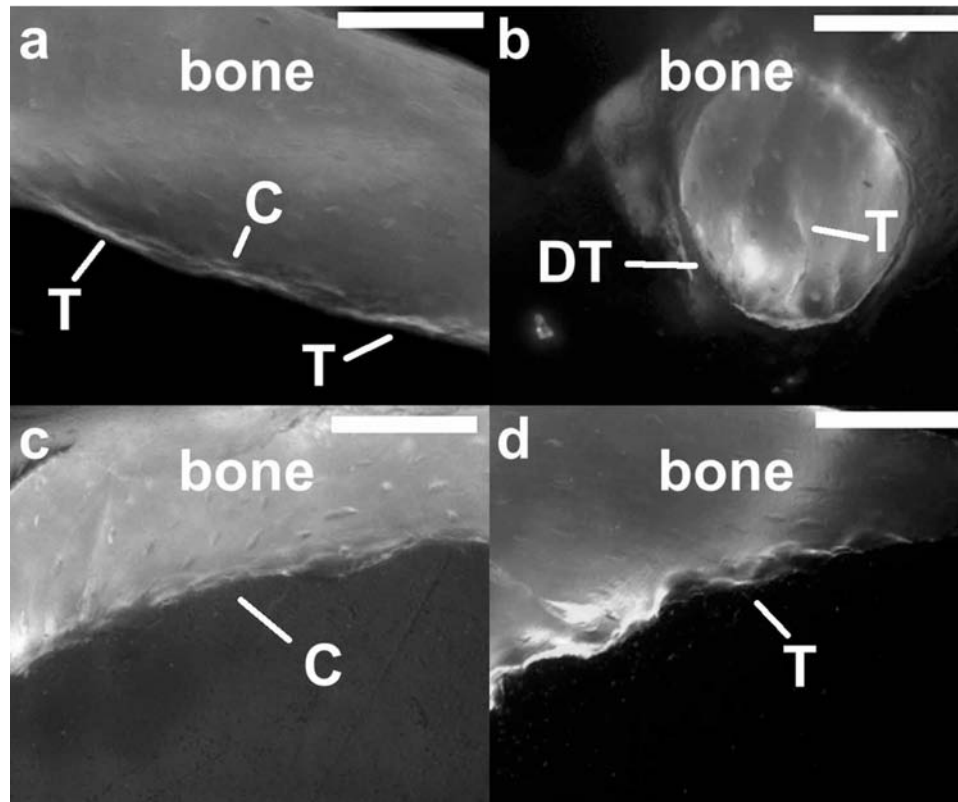
Figure 4. (a) A propagating microcrack. (b) Single microcrack and diffuse damage due to torsion. (c) Cross-hatch microcracks due to compression. (d) Cross-hatch microcracks due to torsion. D: diffuse damage; T: microcrack due to torsion; and C: microcrack due to compression. Scale bar = 100 μm. The loading mode of the microdamage was determined by the color of staining under UV light (O'Brien et al. 2002 2003), which appears as different shades of gray in these images.

from 3.91 ± 1.96 mm^{-2} in the inner region, to 5.08 ± 1.78 mm^{-2} in the intermediate region, and to 5.96 ± 1.92 mm^{-2} in the outer region ($p < 0.0001$). However, the mean density of propagating microcracks did not depend on the region ($p = 0.096$).

Diffuse damage due to compressive overloading was uniform across the specimen, while that due to torsional overloading increased from the axis to the circumference. The diffuse damage area due to compression was 0.0045 ± 0.0014 mm^2/mm^2 independent of region ($p = 0.72$). The diffuse damage area due to the torsional overloading increased from 0.0014 ± 0.0008 mm^2/mm^2 in the inner region, to 0.0037 ± 0.0016 mm^2/mm^2 in the intermediate region, and to 0.0061 ± 0.0024 mm^2/mm^2 in the outer region ($p < 0.0001$, Figure 7b).

Microcracks that initiated during the compressive overloading propagated during the subsequent torsional overloading. On average, 32% of the existing microcracks propagated during torsional loading independent of region ($p = 0.57$, Figure 8). The mean lengths of the microcracks due to compressive and torsional overloading were 57 ± 29 and 54 ± 30 μm, respectively ($p = 0.0005$, Wilcoxon test). In contrast, the mean total length of the microcracks that propagated during torsional overloading was 76 ± 34 μm, which was greater than that for those associated with either compression or torsion alone ($p < 0.0001$, Kruskall–Wallis test, Figure 9). The mean length of microcracks that initiated or propagated during torsion did not depend on the radial region ($p = 0.20$), while the mean length of microcracks that occurred during compression was slightly greater in the intermediate radial region compared to those in the inner and outer regions ($p = 0.0007$).

Discussion

The goal of this study was to investigate the effect of interactions between axial and shear overloading on trabecular bone damage mechanics. At the apparent level, damage, as quantified by decreased Young's and shear moduli, was anisotropic. Axial loading resulted in much larger decreases in the on-axis modulus than in the shear modulus. At the tissue level, interactions were observed in the microdamage accumulation between compressive and torsional overloading. Most notably torsional overloading applied after a compressive overloading caused a high level of microdamage even in the inner region of
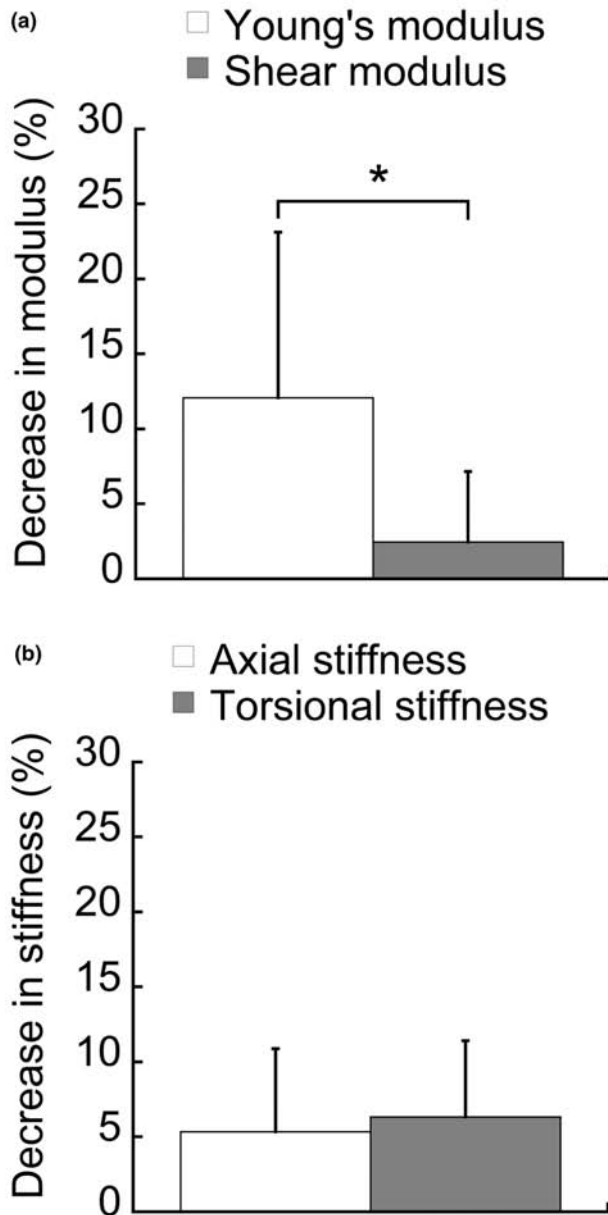
Figure 5. (a) The mean relative decrease of Young's modulus was much greater than that of the shear modulus following compressive overloading ($p = 0.0009$, Wilcoxon test). (b) The mean relative decreases in the axial and torsional stiffnesses following torsional overloading were not significantly different ($p = 0.42$). The mean decrease was greater than zero in all cases ($p < 0.05$, Wilcoxon signed rank test). Error bars are one standard deviation ($n = 14$).

Figure 6. Both the undamaged (E_o) and damaged (E_d) Young's moduli were linearly correlated with volume fraction (a), as were the undamaged (G_o) and damaged (G_d) shear moduli (b). There was no significant difference between the regressions for E_o and E_d ($p = 0.97$) or between those for G_o and G_d ($p = 0.71$, ANCOVA).

the bone where the shear strain was less than 1.33%, which was only slightly higher than the mean yield strain of these specimens. Many of the microcracks near the specimen axes were extended from pre-existing microcracks that initiated during axial loading, suggesting that microcracks may grow even under relatively low shear strains. These findings have implications on the prediction of whole bone strength following damage accumulation. The aniso-
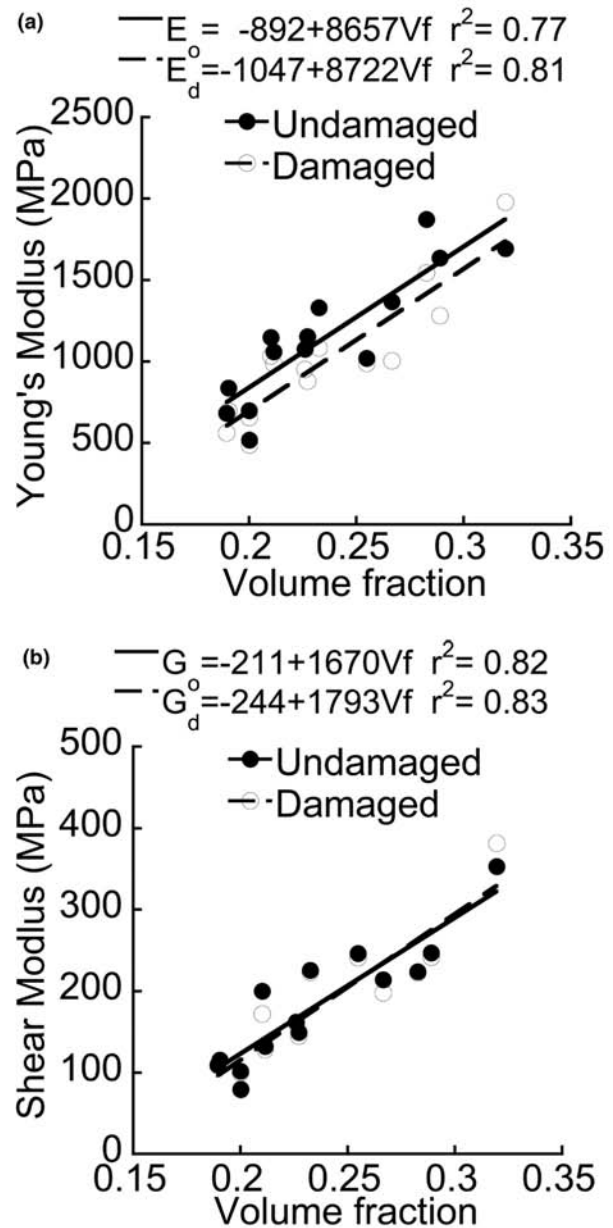
tropy of modulus changes following damage is important, as it would alter the stress field within the trabecular bone, which could in turn decrease the whole bone fracture strength (Kopperdahl et al. 2000). At the same time, pre-existing microcracks due to activities of daily living may increase the susceptibility to microdamage accumulation during off-axis loading events such as a fall, which could precipitate a fracture.
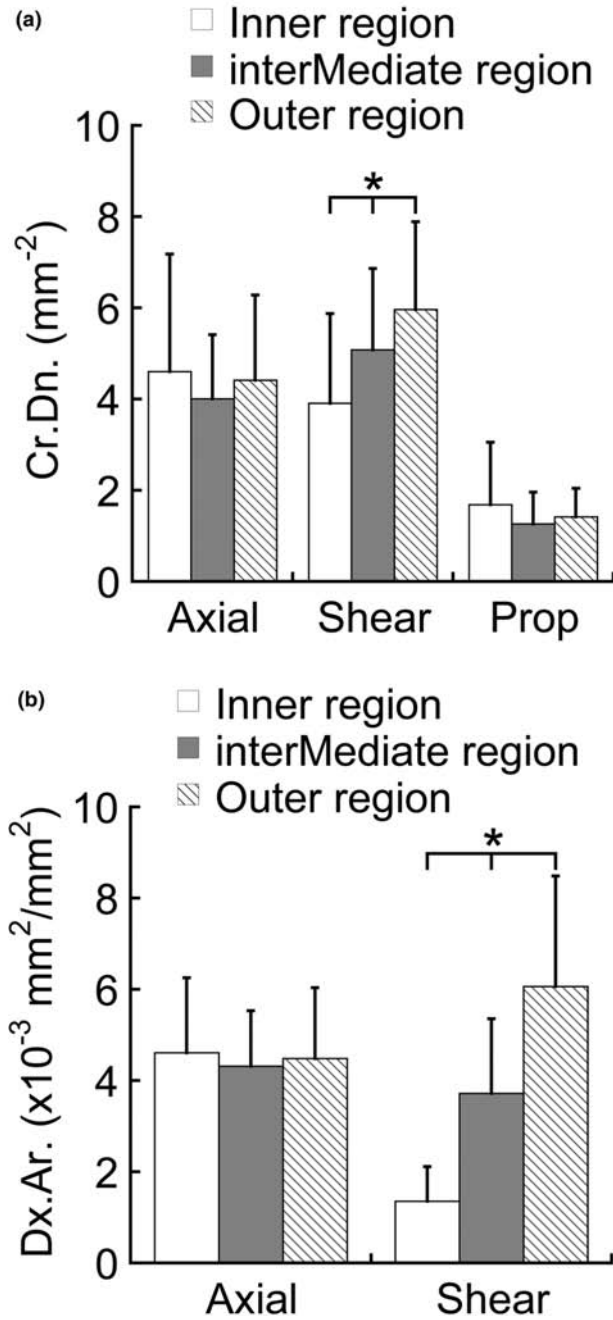
(a)

(b)

Figure 7. (a) The total density of microcracks due to compressive or torsional overloading in the inner (I), intermediate (M), and outer (O) regions. The density of the microcracks due to torsional overloading increased from the inner region to the outer region ($p < 0.05$, two-factor ANOVA). (b) The diffuse damage area was uniform across the specimen during compressive overloading, but increased from the axis to the circumference (and therefore with increasing shear strain) during torsional overloading ($p < 0.05$). Error bars are one standard deviation ($n = 14$).
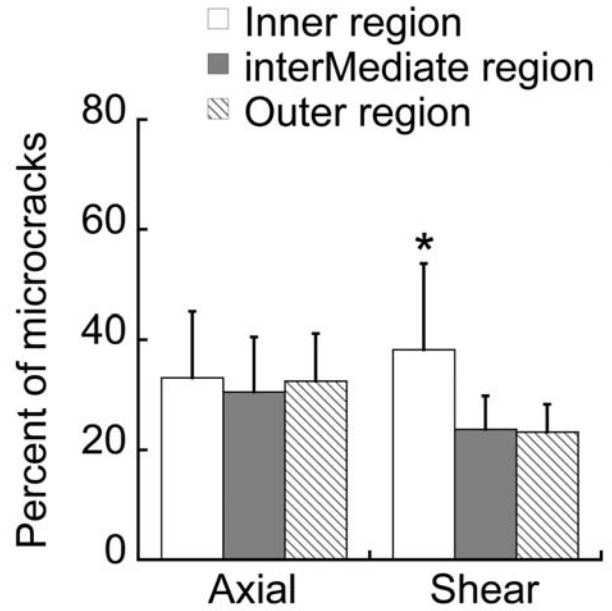

Figure 8. The mean percentage of microcracks that propagated from pre-existing microcracks as a percentage of the total number of microcracks in compression and in torsion (* indicates significant difference, $p < 0.05$, two-factor ANOVA). Error bars are one standard deviation ($n = 14$).
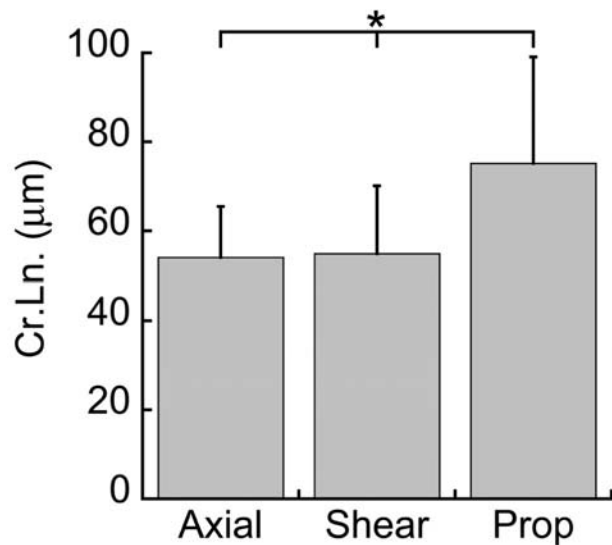

Figure 9. The mean length of the microcracks due to compressive overloading, torsional overloading and those that propagated (* indicates significant difference, $p < 0.0001$, Kruskall–Wallis test). Error bars are one standard deviation ($n = 1776$ axial, 2109 shear, and 596 prop).

This study had several notable strengths. The microdamage accumulation was quantified using a recently developed and novel differential staining technique (O'Brien et al. 2002). Preliminary staining was applied to ensure that damage due to specimen preparation could be differentiated from that which occurred during loading. The changes in the moduli and other mechanical properties were measured using precise mechanical testing methods. As such, the results provide a comprehensive understanding

of damage in dense trabecular bone for on-axis compression and shear loading.

Some limitations should be considered when interpreting the results of this study. First, only one anatomic site was studied in young animals. As such, correlations to architectural parameters were difficult due to limited variations. Further studies in human bone or from multiple anatomic sites may be needed to identify correlations between architecture and microdamage. The relatively high density of bovine tibial bone also limits the direct application of these results to human bone, especially in the case of osteoporosis. However, the architecture and mechanical properties of bovine tibial trabecular bone is similar to that in the healthy human proximal femur (Keaveny et al. 1994a; Morgan & Keaveny 2001). As such, the results provide some insight into the behavior of human bone. The development of microdamage in trabecular bone subjected to only shear loading has not been previously reported, and as such, it is not possible to compare the current results with that case. Knowledge of this behavior would provide better understanding of the unexpectedly high growth and formation of microdamage at low strains. Finally, because the details of the nonlinear mechanical behavior of trabecular bone in shear were not known, it was not possible to calculate the exact changes in modulus following shear loading. This difficulty is inherent to torsional testing of damaging materials. While the stiffness reported here represents an effective modulus, a theoretical constitutive model of damage accumulation is needed to accurately calculate the changes in modulus associated with the measured microdamage.

Overall, our results complement those from previous studies. The elastic moduli reported here were slightly lower than those reported in previous studies (Ford & Keaveny 1996; Keaveny et al. 1994b) for the same type of bone and similar testing methods. However, the strain rate used in this study was only 0.2% per second, compared to 0.5% in previous studies (Ford & Keaveny 1996; Keaveny et al. 1994b), which may affect the stiffness (Linde et al. 1991). In addition, the mean trabecular thickness of the bone used in this study, 187 ± 30 μm, was lower than that reported for previous studies of bovine trabecular bone (Niebur et al. 2001). As such, the difference could also be related to differences in architecture. The mean microcrack density after compressive overloading found here was higher than that found in a previous study for the same strain level (Arthur Moore & Gibson 2002). However, the previous study based microcrack density calculations on the total area of the section. When the reported bone area fractions, which ranged from 0.40 to 0.54, are

considered, the values are comparable to those found here.

The anisotropy of damage behavior in trabecular bone has been recognized by previous investigators. A theoretical model of damage that incorporated anisotropy based on the relationship of the loads to the fabric tensor was developed (Zysset & Curnier 1996). The authors noted that the model was only applicable to monotonic loads, because it did not account for differing modulus changes along the various orthotropic directions. Computational models have shown that the elastic anisotropy ratio changes due to damage, but the orthotropic material coordinate system does not (Liu et al. 2003). The decrease in the shear modulus following axial compressive damage found in this study was even less than that predicted by computer models (Liu et al. 2003), indicating that a more detailed constitutive relationship for the damage behavior is needed for the models to accurately predict damage behavior.

The dependence of the Young's and shear modulus on volume fraction did not change following the axial overloading. As such, detecting damaged trabecular bone by measuring the elastic properties using either *in vitro* or *in situ* techniques may not be possible. The normal variability of trabecular bone mechanical properties with volume fraction obscures the smaller changes due to microdamage accumulation. In particular, the changes in shear modulus following on-axis loading were almost undetectable.

It has been suggested that microcrack development in both trabecular (Arthur Moore & Gibson 2002) and cortical bone (Akkus & Rimnac 2001; Taylor & Prendergast 1997) is limited by microstructural barriers. The mean microcrack length in bovine tibial trabecular bone subjected to a range of strains was related to the distance between lacunae, which was about 85.8 μm (Arthur Moore & Gibson 2002). Our results showed similar behavior for a single loading mode, with 85 and 90% of the initiating microcracks less than 85 μm long following axial compression and torsion, respectively. The microcracks that propagated during torsional loading were longer than those associated with a single loading mode, and only 73% were less than 85 μm long. In this case, the shear strains may cause the microcracks generated during axial compression to change direction and thereby move past microstructural barriers.

Taken together, the results of this study indicate that off-axis loading, such as torsion of cylindrical specimens, can cause growth of existing microcracks as well as initiation of new microcracks. Because microcracks propagated even at low shear strains, the accumulation of microdamage, which appears to be somewhat benign in normal loading, may result in a

gradual increase in fracture susceptibility during off-axis loading due to propagation of existing micro-cracks.

References

Akkus O, Rimnac CM. 2001. Cortical bone tissue resists fatigue fracture by deceleration and arrest of microcrack growth. J Biomech 34:757–764.

Arthur Moore TL, Gibson LJ. 2002. Microdamage accumulation in bovine trabecular bone in uniaxial compression. J Biomech Eng 124:63–71.

Carter DR, Hayes WC. 1977. The compressive behavior of bone as a two-phase porous structure. J Bone Joint Surg 59-A:954–962.

Fazzalari NL, Forwood MR, Manthey BA, Smith K, Kolesik P. 1998a. Three-dimensional confocal images of microdamage in cancellous bone. Bone 23:373–378.

Fazzalari NL, Forwood MR, Smith K, Manthey BA, Herreen P. 1998b. Assessment of cancellous bone quality in severe osteoarthrosis: Bone mineral density, mechanics, and micro-damage. Bone 22:381–388.

Fenech C, Keaveny TM. 1999. A cellular solid criterion for predicting the axial-shear failure properties of trabecular bone. J Biomech Eng 121:414–422.

Ford CM, Keaveny TM. 1996. The dependence of shear failure properties of bovine tibial trabecular bone on apparent density and trabecular orientation. J Biomech 29:1309–1317.

Fuller GF. 2000. Falls in the elderly. Am Fam Physician 61:2159–2168, 2173–2174.

Fyhrie DP, Schaffler MB. 1994. Failure mechanisms in human vertebral cancellous bone. Bone 15:105–109.

Galante J, Rostoker W, Ray RD. 1970. Physical properties of trabecular bone. Calcif Tissue Res 5:236–246.

Gregg EW, Kriska AM, Salamone LM, Roberts MM, Anderson SJ, Ferrell RE, Kuller LH, Cauley JA. 1997. The epidemiology of quantitative ultrasound: a review of the relationships with bone mass, osteoporosis and fracture risk. Osteoporos Int 7:89–99.

Gregg EW, Pereira MA, Caspersen CJ. 2000. Physical activity, falls, and fractures among older adults: A review of the pidemiologic evidence. J Am Geriatr Soc 48:883–893.

Hoshaw SJ, Cody DD, Saad AM, Fyhrie DP. 1997. Decrease in canine proximal femoral ultimate strength and stiffness due to fatigue damage. J Biomech 30:323–329.

Keaveny TM, Pinilla TP, Crawford RP, Kopperdahl DL, Lou A. 1997. Systematic and random errors in compression testing of trabecular bone. J Orthop Res 15:101–110.

Keaveny TM, Wachtel EF, Ford CM, Hayes WC. 1994a. Differences between the tensile and compressive strengths of bovine tibial trabecular bone depend on modulus. J Biomech 27:1137–1146.

Keaveny TM, Wachtel EF, Guo XE, Hayes WC. 1994b. Mechanical behavior of damaged trabecular bone. J Biomech 27:1309–1318.

Kopperdahl DL, Pearlman JL, Keaveny TM. 2000. Biomechanical consequences of an isolated overload on the human vertebral body. J Orthop Res 18:685–690.

Lee TC, Myers ER, Hayes WC. 1998. Fluorescence-aided detection of microdamage in compact bone. J Anat 193:179–184.

Linde F, Norgaard P, Hvid I, Odgaard A, Soballe K. 1991. Mechanical properties of trabecular bone. Dependency on strain rate. J Biomech 24:803–809.

Linde F, Sorensen HC. 1993. The effect of different storage methods on the mechanical properties of trabecular bone. J Biomech 26:1249–1252.

Liu X, Wang X, Niebur GL. 2003. Effects of damage on the orthotropic matrerial symmetry of bovine tibial trabecular bone. J Biomech 36:1753–1759.

Mashiba T, Hirano T, Turner CH, Forwood MR, Johnston CC, Burr DB. 2000. Suppressed bone turnover by bisphosphonates increases microdamage accumulation and reduces some biomechanical properties in dog rib. J Bone Miner Res 15:613–620.

Mashiba T, Turner CH, Hirano T, Forwood MR, Johnston CC, Burr DB. 2001. Effects of suppressed bone turnover by bisphosphonates on microdamage accumulation and biome-chanical properties in clinically relevant skeletal sites in beagles. Bone 28:524–531.

Morgan EF, Keaveny TM. 2001. Dependence of yield strain of human trabecular bone on anatomic site. J Biomech 34:569–577.

Mori S, Harruff R, Ambrosius W, Burr DB. 1997. Trabecular bone volume and microdamage accumulation in the femoral heads of women with and without femoral neck fractures. Bone 21:521–526.

Nadai A. 1950. Torsion of a round bar. The stress-strain curve in shear. In: Nadai A, editors. Theory of flow and fracture of solids. New York: McGraw-Hill. p 347–352.

Niebur GL, Yuen JC, Burghardt AJ, Keaveny TM. 2001. Sensitivity of damage predictions to tissue level yield properties and apparent loading conditions. J Biomech 34:699–706.

O'Brien FJ, Taylor D, Lee TC. 2002. An improved labelling technique for monitoring microcrack growth in compact bone. J Biomech 35:523–526.

O'Brien FJ, Taylor D, Lee TC. 2003. Microcrack accumulation at different intervals during fatigue testing of compact bone. J Biomech 36:973–980.

Taylor D, Prendergast PJ. 1997. A model for fatigue crack propagation and remodeling in compact bone. Proc Inst Mech Eng H 211:369–375.

Van Rietbergen B, Odgaard A, Kabel J, Huiskes R. 1996. Direct mechanics assessment of elastic symmetries and properties of trabecular bone architecture. J Biomech 29:1653–1657.

Vashishth D, Koontz J, Qiu SJ, Lundin-Cannon D, Yeni YN, Schaffler MB, Fyhrie DP. 2000. *In vivo* diffuse damage in human vertebral trabecular bone. Bone 26:147–152.

Wachtel EF, Keaveny TM. 1997. Dependence of trabecular damage on mechanical strain. J Orthop Res 15:781–787.

Wang X, Liu X, Niebur GL. 2004. Preparation of on-axis cylindrical trabecular bone specimens using micro-CT imaging. J Biomech Eng 126:122–125.

Wenzel TE, Schaffler MB, Fyhrie DP. 1996. *In vivo* trabecular microcracks in human vertebral bone. Bone 19:89–95.

Yeni YN, Hou FJ, Ciarelli T, Vashishth D, Fyhrie DP. 2003. Trabecular shear stresses predict *in vivo* linear microcrack density but not diffuse damage in human vertebral cancellous bone. Ann Biomed Eng 31:726–732.

Zysset PK, Curnier A. 1996. A 3D damage model for trabecular bone based on fabric tensors. J Biomech 29:1549–1558.